The Astrophysical Journal, 881:131 (15pp), 2019 August 20 https://doi.org/10.3847/1538-4357/ab2984

Lyα Halos around $z \sim 6$ Quasars

Alyssa B. Drake[1], Emanuele Paolo Farina[1,2], Marcel Neeleman[1], Fabian Walter[1], Bram Venemans[1], Eduardo Banados[1], Chiara Mazzucchelli[3], and Roberto Decarli[4]
[1] Max Planck Institute for Astronomy, Konigstuhl, Heidelberg, Germany; drake@mpia.de
[2] Max Planck Institute for Astrophysics, Karl-Schwarzschild-Str, Garching, Germany
[3] European Southern Observatory, Alonso de Cordova 3107, Vitacura, Region Metropolitana, Chile
[4] INAF—Osservatorio Astronomico di Bologna, Via Piero Gobetti, 93/3, I-40129 Bologna BO, Italy
Received 2019 May 14; revised 2019 June 7; accepted 2019 June 11; published 2019 August 21

Abstract

We present deep MUSE observations of five quasars within the first Gyr of the universe ($z \gtrsim 6$), four of which display extended Lyα halos. After PSF subtraction, we reveal halos surrounding two quasars for the first time, as well as confirm the presence of two more halos for which tentative detections exist in long-slit spectroscopic observations and narrowband imaging. The four Lyα halos presented here are diverse in morphology and size, they each display spatial asymmetry, and none are centered on the position of the quasar. Spectra of the diffuse halos demonstrate that none are dramatically offset in velocity from the systemic redshift of the quasars ($\Delta v < 200\,\mathrm{km\,s^{-1}}$); however. each halo shows a broad Lyα line, with a velocity width $\sim$1000 $\mathrm{km\,s^{-1}}$. Total Lyα luminosities range between $\sim 2 \times 10^{43}$ and $\sim 2 \times 10^{44}$ $\mathrm{erg\,s^{-1}}$, reaching maximum radial extents of 13–30 pkpc from the quasar positions. We find larger sizes and higher Lyα luminosities than previous literature results at this redshift, but find no correlation between the quasar properties and the Lyα halo, suggesting that the detected emission is most closely related to the physical properties of the circumgalactic medium.

Key words: galaxies: active – galaxies: formation – galaxies: halos – galaxies: high-redshift – quasars: emission lines – quasars: general – quasars: individual (J2228+0110, J2100–1715, J1030+0524, J2329–0301, P231–20)

1. Introduction

The importance of studying the gas immediately surrounding galaxies has long been understood. In particular, as the circumgalactic medium (CGM) lies at the interface between the galaxies themselves and the diffuse hydrogen in the intergalactic medium (IGM), it holds the key to understanding some of the most fundamental concepts of galaxy formation and evolution (e.g., Tumlinson et al. 2017). Until recently, the most prudent method of studying this diffuse medium relied on absorption features imprinted on the spectra of distant quasars by intervening gas. For instance, Hennawi et al. (2006), Hennawi & Prochaska (2007), and Farina et al. (2013, 2014) used this technique to study the CGM around other quasars along the line of sight.

Studying the CGM in emission, however, is a greater challenge. Nonetheless, in recent years the detection of Lyα halos around quasars at lower redshift (e.g., $3 \leqslant z \leqslant 4$) has become almost routine, in large part thanks to advances in instrumentation such as ESO's Multi-Unit Spectroscopic Explorer (MUSE; Bacon et al. 2010) on the Very Large Telescope (VLT). MUSE has allowed us to enter the paradigm whereby extended Lyα emission is ubiquitous not only around active galaxies (Cantalupo et al. 2014; Borisova et al. 2016; Arrigoni Battaia et al. 2019) but also normal star-forming galaxies out to $z \sim 6$ (Wisotzki et al. 2016; Drake et al. 2017a, 2017b; Leclercq et al. 2017).

The study of quasars in the first Gyr of the universe ($z \gtrsim 6$) is a probe through which we can directly observe young galaxies and their black holes during their most rapid growth period. In addition, ionizing radiation from the active galactic nucleus (AGN) can actually aid in the detection of CGM gas by causing it to shine more brightly in Lyα. Furthermore, as large amounts of gas are directly funnelled onto the quasars' black holes, the accretion disks are luminous enough to allow their detection out to at least $z = 7.5$ (Bãnados et al. 2018) with the current facilities, allowing us to probe sources of ionizing photons, and the gas fueling their growth, well into the epoch of reionization.

To date, a handful of detections of extended Lyα emission around very-high-redshift quasars ($z \sim 6$) have been reported. Roche et al. (2014) presented long-slit spectroscopy of the radio-loud quasar J2228+0110 at a redshift of $z = 5.903$ (see also Zeimann et al. 2011). At present, this remains the highest-redshift radio-loud quasar to show signs of extended Lyα emission. The $z = 6.43$ quasar J2329−0301 (Goto et al. 2009) is another example for which multiple measurements of a Lyα halo have been reported in the literature. Following its detection in narrowband imaging, the halo was spectroscopically confirmed in Willott et al. (2011) and Goto et al. (2012) and in these long-slit studies, the halo around J2329−0301 appeared very similar to J2228+0110 in terms of size and luminosity. Finally, Farina et al. (2017) targeted the $z = 6.61$ QSO J0305−3150 with MUSE. With one of the highest SFRs and Eddington ratios above $z \sim 6$, this quasar provides an ideal source to target a large gas reservoir surrounding one of the first QSOs. Farina et al. (2017) detected a faint Lyα halo around J0305−3150 extending ∼9 pkpc, offset in velocity by 155 $\mathrm{km\,s^{-1}}$, and with a total luminosity of $(3.0 \pm 0.4) \times 10^{42}$ $\mathrm{erg\,s^{-1}}$.

Motivated by these studies, we search for Lyα halos in the deepest available MUSE observations of the highest-redshift quasars ($z \sim 6$). To reach approximately the surface-brightness (SB) level achieved in Farina et al. (2017), we queried the ESO archive for observations of exposure time ∼2 hr or greater, resulting in a total sample of five objects listed in Table 1. SB levels in the wavelength layer where Lyα emission peaks range between 4.71×10^{-19} $\mathrm{erg\,s^{-1}\,cm^{-2}\,arcsec^{-2}}$ and 8.81×10^{-19} $\mathrm{erg\,s^{-1}\,cm^{-2}\,arcsec^{-2}}$ (see Table 2 for details). The observations include two objects with evidence for extended

Table 1
QSOs for which Archival MUSE Data Are Presented in This Paper

QSO	R.A.	Decl.	Discovery	z	z Method	z Reference
J2228+0110	22:28:43.535	+01:10:32.2	Zeimann et al. (2011)	5.903	Lyα	Roche et al. (2014)
J2100−1715	21:00:54.616	−17:15:22.50	Willott et al. (2010a)	6.081	[C II]	Decarli et al. (2018)
J1030+0524	10:30:27.098	+05:24:55.00	Fan et al. (2001a)	6.308	Mg II	Kurk et al. (2007)
J2329−0301	23:29:08.275	−03:01:58.80	Willott et al. (2007)	6.417	Mg II	Willott et al. (2011)
P231−20	15:26:37.841	−20:50:00.66	Mazzucchelli et al. (2017b)	6.587	[C II]	Decarli et al. (2018)

Note. In the first four columns we list the object name, coordinates, and the reference for the discovery spectrum of each object. In column 5 we list the current best estimate of each quasar's systemic redshift, in column 6 we give the method via which the systemic redshift was measured, and in column 7 we give the appropriate literature reference for the redshift measurement.

Table 2
Total Fluxes and Luminosities for the Five QSOs Discussed in This Work

QSO	Total Flux (erg s^{-1} cm^{-2})	log LLya (erg s^{-1})	Maximum Extent (arcsec)	Maximum Extent (pkpc)	NB Width (N) (Angstroms)	SB Lyα (1σ) (erg s^{-1} cm^{-2} arcsec^{-2})	SB NB (1σ) (erg s^{-1} cm^{-2} arcsec^{-2})
J2228+0110	4.64×10^{-16}	44.250	5.1	29.1	8355-8435 (64)	5.03×10^{-19}	6.43×10^{-18}
J2100−1715	...	...	...	...	8600-8650 (40)	6.45×10^{-19}	4.84×10^{-18}
J1030+0524	4.28×10^{-17}	43.282	2.8	15.7	8865–8900 (28)	4.71×10^{-19}	3.23×10^{-18}
J2329−0301	1.49×10^{-16}	43.841	2.2	12.2	9000–9045 (36)	7.40×10^{-19}	6.80×10^{-18}
P231−20	1.77×10^{-16}	43.942	3.4	18.1	9210–9260 (32)	8.81×10^{-19}	7.11×10^{-18}

Note. In the first, second, and third columns we object name, our measurement of the total flux, and corresponding log luminosity. These are the values summed within our measurement of the maximum extent of the halos on-sky. Columns 4 and 5 report the maximum radial extent we measure for each QSO, in arcseconds, and pkpc at the respective QSO redshifts. In the sixth column we give the wavelength range and width (Å) over which the measurements were made. In the final two columns we give the 1σ surface-brightness limits first in the wavelength layer where the peak of the Lyα emission is detected, and then in the narrowband image constructed from the wavelength range listed in column 6.

Lyα emission from long-slit spectra (Willott et al. 2011; Goto et al. 2012; Roche et al. 2014) or narrowband imaging (Momose et al. 2019).

Our analysis proceeds as follows. In Section 2 we provide context and notes on previous observations of quasars in our study, and in Section 3 we describe our data reduction procedure and PSF subtraction technique. We present our results in Section 4, beginning with MUSE images and spectra of each QSO. We then show our PSF-subtracted data and estimate total fluxes and maximum extents of Lyα halos (where present). We next analyze the data cubes to a uniform surface-brightness limit, and assess the morphology, spatial offsets, velocity offsets, and integrated line profiles. Finally, we include spatially resolved analyses of the kinematic structure of each halo. In Section 5 we discuss our measurements within the context of the literature, and speculate on the presence of evolution in the CGM, and the mechanisms powering the Lyα emission.

Throughout this paper we use the terms "quasar" and "QSO" interchangeably, and assume a ΛCDM cosmology with $\Omega_m = 0.3$, $\Omega_\Lambda = 0.7$, and $h = 70\,\mathrm{km\,s^{-1}}$.

2. Previous Observations

In Table 1 we summarize from the literature some basic properties of the QSOs analyzed here.

2.1. J2228+0110

J2228+0110, at $z = 5.903$, was discovered via its radio emission as part of the Stripe82 VLA survey (peak flux density 0.31 mJy; Zeimann et al. 2011). J2228+0110 is optically faint, however, with $M_{1450} = -24.53$, and consequently its radio-loudness parameter is high, $R \sim 1100$. With an LRIS spectrum, Zeimann et al. (2011) measured the velocity width of the Lyα line in the QSO spectrum to be $1890\,\mathrm{km\,s^{-1}}$. Roche et al. (2014) returned to J2228+0110 with GTC-OSIRIS, and were the first to detect signs of an extended Lyα halo around the quasar. They measured a velocity width of the Lyα line (including QSO) of $1189 \pm 24\,\mathrm{km\,s^{-1}}$. In addition they extracted an offset spectrum toward the southwest of the quasar, and measured a flux of $2.02 \pm 0.46 \times 10^{-17}\,\mathrm{erg\,s^{-1}\,cm^{-2}}$, with a peak of emission at 8386.26 ± 2.41 Å. The Lyα luminosity of the halo was constrained to be $L(\mathrm{Ly}\alpha) \leqslant 7.8 \times 10^{42}\,\mathrm{erg\,s^{-1}}$ extended for "at least" 9 pkpc. J2228+0110 is the only known radio-loud object in this sample. MUSE date for this object total 11.30 hr (PI: Roche).

2.2. J2100−1715

J2100−1715 was uncovered as part of the Canada–France-High-z-Survey and reported in Willott et al. (2010b); it has an $M_{1450} = -25.55$ (Bañados et al. 2016). It was targeted as one of 27 $z \sim 6$ quasars in the [C II] survey of Decarli et al. (2018). MUSE data were taken for this object (PI: Decarli), amounting to 3.70 hr in total.

2.3. J1030+0524

J1030+0524 at $z = 6.304$ (Fan et al. 2001b) was one of the earliest quasars to be discovered at $z \sim 6$ in the Sloan Digital Sky Survey (SDSS), and has an $M_{1450} = -26.99$ (Bañados et al. 2016). Decarli et al. (2012) found no halo for this quasar

in their Subaru narrowband imaging. MUSE data are of integration time 6.43 hr (PI: Karman).

2.4. J2329−0301

J2329−0301 ($z = 6.417$) was discovered as part of the Canada–France High-z Quasar Survey (CFHQS; Willott et al. 2007), and has $M_{1450} = -25.25$ (Bañados et al. 2016). Goto et al. (2009) were the first to find evidence of an extension to the Lyα emission, tentatively seen in Subaru/Suprime-Cam narrowband imaging—they estimated an extent of 4″ on the sky. The presence of the halo was confirmed in the long-slit spectroscopy of Willott et al. (2011) (measuring 8×10^{43} erg s^{-1} over 15 pkpc or 2.″7) and Goto et al. (2012) (1.7×10^{43} erg s^{-1} over 4″), and subsequently further narrowband imaging in Momose et al. (2019) (1.5×10^{44} erg s^{-1} over 6.″9 in diameter). This quasar was observed as part of MUSE Science Verification, with an integration time of 2 hr.

2.5. P231−20

P231−20 is the highest-redshift object in our study, at $z = 6.586$, discovered by Mazzucchelli et al. (2017b). This quasar is one of the brightest known at $z > 6.5$; $M_{1450} = -27.20$ (Bañados et al. 2016); and is known to have a very close companion galaxy detected in [C II], and reported in Decarli et al. (2017). MUSE data were taken as part of a program (PI: Farina), with a total integration time of 3.20 hr.

3. MUSE Observations and Analysis

We analyzed the deepest available MUSE data for quasars at $z \sim 6$. A summary of the sample is given in Table 1.

3.1. Data Reduction

MUSE data and raw calibrations were downloaded from the ESO archive for each of the quasars listed in Table 1. We used the MUSE Data Reduction Software (version 2.4.1) to reduce each individual exposure, combining them into deep data cubes for each object. Once the date were fully reduced we ran the Zurich Atmospheric Purge software (ZAP; Soto et al. 2016) to perform additional sky subtraction. On these final "ZAPped" data cubes we perform the remainder of our analysis.[5]

3.2. PSF Subtraction

The detection of low-surface-brightness emission around a bright point source requires removing the contribution of light from the unresolved object. This is achieved by characterizing the point-spread function (PSF) in the data, typically using a bright star in the field, or in the case of a quasar, using the spectral continuum from the quasar itself. The quasar continuum is dominated by light from the accretion disk of the AGN, which is an unresolved source at the resolution of MUSE. For each QSO in this work we construct our model of the PSF following the steps outlined below. We utilize the simultaneous spatial and spectral information in the MUSE datacube to collapse several spectral layers of the quasar continuum, creating a "PSF image." Using the quasar itself allows us to avoid issues related to PSF variations across the field, and spatial interpolation. Indeed, in the analysis of the $z \sim 6$ quasar presented in Farina et al. (2017), these two commonly applied PSF subtraction techniques were tested and found to be equally reliable.

In constructing our PSF image, two considerations help produce the most reliable results. First, the need for signal-to-noise (S/N) in the PSF image means including as wide a spectral range as possible; however, at these wavelengths (particularly >7000 Å) emission from the night sky varies rapidly as a function of wavelength, resulting in differences in the noise properties of adjacent wavelength layers even after careful sky subtraction. This means that the S/N in the PSF image is actually improved by excluding the wavelength layers of the cube that are most affected by sky lines.

The wavelength layers chosen to construct the PSF image for each quasar are highlighted in pink on the spectrum shown in Figure 1.[6] We then work systematically through each wavelength layer of the cube, scaling the flux in the peak pixel of the PSF image to the flux of the QSO in the same spatial pixel, and subtracting the scaled PSF image from the datacube wavelength layer. This way we produce an entire PSF-subtracted datacube.[7]

Once the PSF-subtracted datacube has been created, we mask an ellipse of dimensions equal to the Gaussian-equivalent PSF (the FWHM of a two-dimensional Gaussian fit to the PSF image) in each wavelength layer, and exclude this central region from further analysis, as it is likely to contain complex residuals.

4. Results

We present the MUSE data for each QSO, together with the analysis of the PSF-subtracted data cubes, in the subsections below.

4.1. Images and Spectra

In Figure 1 we show MUSE images and spectra for each QSO. The first panel shows a narrowband image ($\Delta\lambda = 120$ Å) centered on the predicted position of the Lyα line from our best estimate of the quasar systemic redshift. In the second panel we show the "PSF image" constructed as described in Section 3.2, and in the third panel we show the quasar spectrum extracted in an aperture of 2″ in diameter. The wavelength range of each image is highlighted on the spectrum, and likewise the extraction aperture of the spectrum is shown on each image.

4.2. Lyα Halos at z $\sim$ 6

We detect extended Lyα emission around four out of five quasars in the PSF-subtracted data cubes. We proceed now by estimating the total fluxes of the halos, and maximum extents that the diffuse emission reaches from the positions of the quasars. In order to correctly measure the extent and luminosity of the Lyα halos, we need to cover the full spectral width of the Lyα line. As a result, for each quasar we use a different spectral range and hence each pseudo-narrowband reaches a different surface-brightness limit. The wavelength layers that comprise

[5] We note that in parallel to this analysis we assessed the "un-ZAPped" data cubes, finding consistent results.

[6] We note that in the case of P231−20, the PSF image was by necessity constructed using wavelength layers of the cube that could contain the high-velocity tails of Lyα emission. This might lead to a slight oversubtraction of the halo, therefore our flux estimate is a conservative one.

[7] To test the reliability of the PSF image scaling we also conducted a test using the average value of 5 pixels in the center of the PSF image scaled to that of 5 pixels at the center of the QSO, and verified that our results did not change.

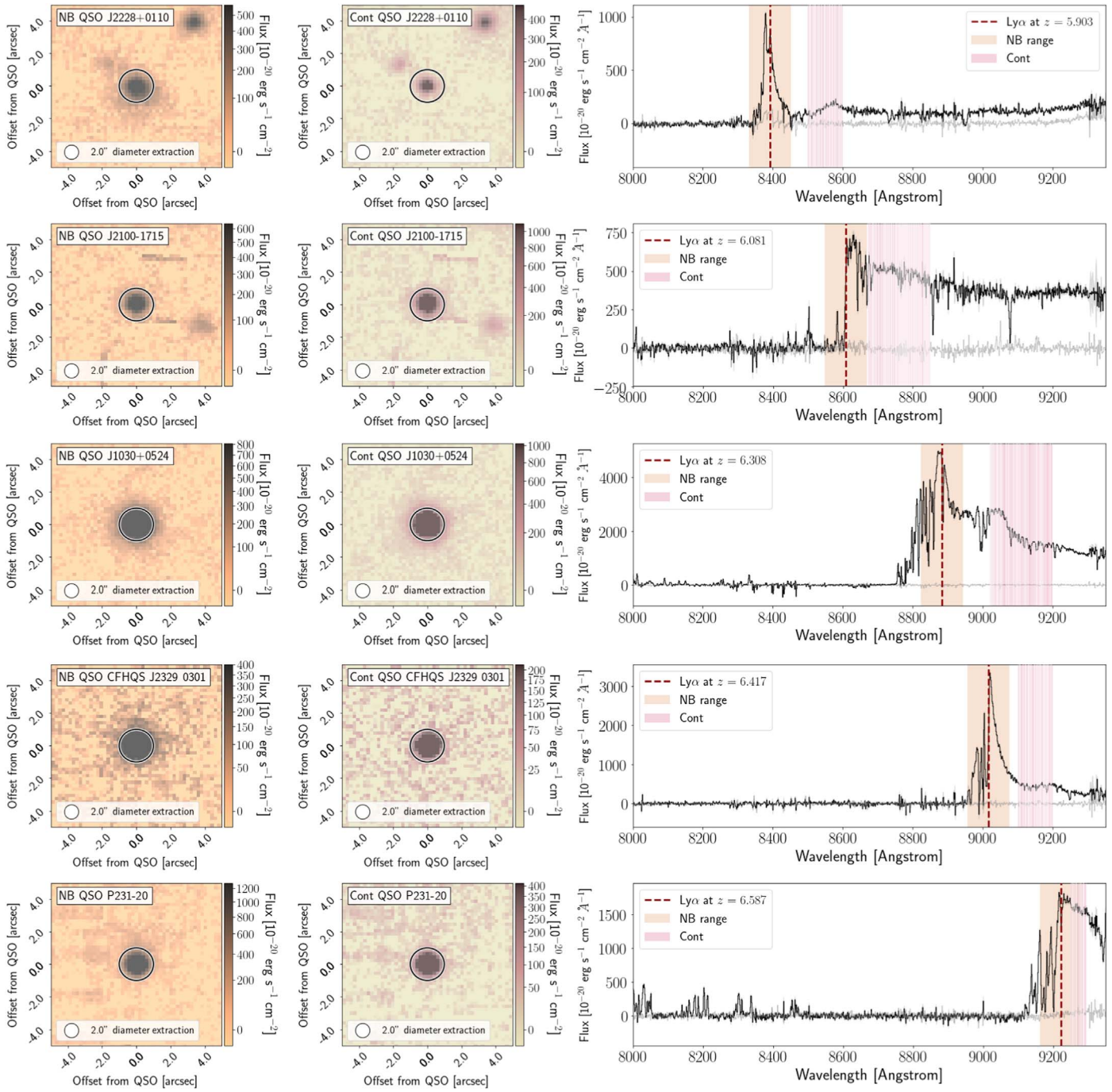

Figure 1. MUSE images and spectra of the five $z \sim 6$ QSOs analyzed here. The left panels show fixed-width narrowband images of $\Delta\lambda = 120$ Å centered on the predicted wavelength of Lyα from our best estimate of the systemic redshift (see Table 1). The wavelength range of each narrowband image is highlighted by the orange region on the spectrum. In the central panels we show the "clean" continuum images, i.e., collapses of the QSO continuum emission, constructed using wavelength layers of the cube where night sky emission is low (see Section 3.2 for details). The layers combined to make the image are highlighted in pink on the spectrum. In the final column, we show the QSO spectrum extracted in an aperture of 2″ in diameter, the extraction region is given by the white circle on the narrowband and continuum-collapse images. The dashed red lines on the spectrum give the predicted peak wavelength of the Lyα emission according to the systemic redshift.

each of these narrow bands are shown in Appendix A (Figure 10), and their corresponding 1σ surface-brightness limits are listed in Table 2. In order to facilitate comparison between the halos we will also analyze the data to a uniform surface-brightness limit in Section 4.3 to assess the "bulk" properties of the halos, i.e., morphology, spatial offset of the emission peak from the quasar, and the integrated velocity offset and velocity widths of the halos. Finally, in Section 4.3.3 we employ a S/N cut *per voxel* in order to produce the most sensitive maps of the kinematic structure of each halo; details follow in Section 4.3.3.

4.2.1. Total Lyα Fluxes and Maximum Extents

We begin by visually inspecting the PSF-subtracted data cubes, and extracting a spectrum in a large aperture chosen by

eye to encapsulate the visible extended emission (typically 6″ in diameter; see the Appendix). From this spectrum we then choose the appropriate spectral window over which to collapse the cube to encapsulate the entire spectral width of the Lyα line, resulting in our preferred pseudo-narrowband image.

In accordance with other works in the literature (e.g., Borisova et al. 2016; Wisotzki et al. 2016; Drake et al. 2017a, 2017b; Arrigoni Battaia et al. 2019) we use azimuthally averaged profiles on these fixed-width narrowband images in order to track the curve of growth of the extended emission around each object, and sum the Lyα flux within the radius where the light profile hits the background of the observations. Our best estimates of the total flux of each PSF-subtracted halo are presented in Table 2, together with the wavelength layers over which the estimate was made, the maximum extent of the emission, and the corresponding total Lyα luminosity of each halo. We display the narrowband images and light profiles in Figure 2.

By far, the most prominent halo is that around radio-loud J2228+0110, extending 5.1 arcsec (or 29.1 pkpc), making it to date the largest halo detected around a $z \sim 6$ quasar. We measure the total flux of the halo as 4.64×10^{-16} erg s^{-1} cm^{-2} across this extent, a larger flux than any of the existing literature measurements. Roche et al. (2014), for example, measured a halo flux of $2.02 \pm 0.46 \times 10^{-17}$ erg s^{-1} cm^{-2}, thus our estimate is an order of magnitude larger than previous measurements. This is likely to be due to very different observational techniques—Roche et al. (2014) estimated the halo flux in a long-slit offset from the position of the quasar, confirming the presence of extended emission, but by no means an observation designed to precisely measure the halo flux.

J2100−1715, the next highest-redshift object shows no sign of extended emission above the SB limit in these data (4.84×10^{-18} erg s^{-1} cm^{-2} arcsec^{-2}) in our narrowband collapse around the Lyα line.

J1030+0524 shows a small but distinct halo toward the West extending 2.″8 or 15.7 pkpc from the position of the quasar. Within this radius we measure a total flux of 4.28×10^{-17} erg s^{-1} cm^{-2}.

J2329−0301 is the only quasar other than J2228+0110 to have previous measurements of an extended Lyα halo. We detect a halo as much as Goto et al. (2009, 2012), Willott et al. (2011), and Momose et al. (2019) do, extending north. In our data the halo reaches a maximum radial extent of 2.″2 or 12.2 pkpc, with a total halo flux of 1.49×10^{-16} erg s^{-1} cm^{-2}. Interestingly, our halo luminosity estimate is very similar to that of Momose et al. (2019), although Momose et al. (2019) found a larger extension on-sky (6.″9 in diameter in an image reaching an SB limit of 4×10^{-18} erg s^{-1} cm^{-2} arcsec^{-2} at the 3σ level.). These differences are probably due to the image produced in this work being sensitive only to a higher SB limit (e.g., a 1σ limit of 6.80×10^{-18} erg s^{-1} cm^{-2} arcsec^{-2} as quoted in Table 2) meaning the halo is less well-detected at its outskirts, but conversely the ability of MUSE to encapsulate the spectral width of the line very precisely (compared to narrowband flux losses) means that we recover approximately the same total flux/luminosity.

Finally, we see a Lyα halo around P231−20 extending 3.″4, or 18.1 pkpc, with an extent similar to that of J1030+0524, but with a total flux of 1.77×10^{-16} erg s^{-1} cm^{-2}, approximately twice the flux of J1030+0524 (making it comparable in flux to J2329−0301). In Table 2 we report our best estimate of the maximum radial extent that each halo reaches from the position of the quasar, hitting SB background levels between 3.23×10^{-18} and 7.11×10^{-18} erg s^{-1} cm^{-2} arcsec^{-2}. All four of the halos have total Lyα luminosities greater than $L_{\mathrm{Ly}\alpha} = 1 \times 10^{43}$ erg s^{-1}; we will return to the halo luminosities in the context of other works in Section 5.

4.3. Properties of Diffuse Lyα above a Uniform Surface-brightness Limit

In literature searches, authors frequently survey objects to a uniform depth and consider only emission above some S/N or surface-brightness level. In the data analyzed here, the observations reach various depths (summarized in Table 2), so in order to directly compare emission around the quasars we must compare the properties of the diffuse emission to a depth easily reached in all the observations. In Figure 3 we present the same narrowband images described above, now in surface-brightness units, and smoothed with a Gaussian kernel of 1.2 pixels to emphasize the morphology of the halos. The images are contoured at 1.0×10^{-17} and 7.5×10^{-18} erg s^{-1} cm^{-2} arcsec^{-2} to highlight the brightest emission around each source.

We discuss below our analysis of the morphology and emission-line properties of each halo, and summarize our findings in Table 3.

4.3.1. Nebula Morphology and Spatial Offsets

It is evident from Figure 3 that the extended emission around the four QSOs showing a Lyα halo is diverse in appearance and size. With the possible exception of J2329−0301, the halos are not centered on the spatial position of the QSOs, and none appear regular in shape.

We compute for each object the spatial offset between the position of the QSO and the peak of the halo emission (see Table 3). In Figure 3 we overlay a white cross at the position of the QSO, and a cyan cross at the peak of the halo emission in each panel. The halos are on average offset by 0.″77 (4.3 pkpc across their respective redshifts). Interestingly, the halo most removed from its associated QSO is radio-quiet, and is the highest-redshift object in our sample, P231−20, which is also known to have a close companion (Decarli et al. 2017).

We also list in Table 3 the area in square arcseconds of the SB $> 10^{-17}$ erg s^{-1} cm^{-2} arcsec^{-2} emission in this maximal S/N image.

4.3.2. Velocity Offsets and Integrated Line Profiles

We consider the kinematic properties of the halos in two ways, beginning with the integrated properties of the halos. First, in Figure 4 we show spectra of the quasar (upper panels), and those of the diffuse halo emission after PSF subtraction (lower panels).

Spectra of the halos are extracted in apertures of 3″ in diameter, but excluding the central region (PSF).

Overall, the halos show little velocity offset from their respective QSOs, either with respect to the systemic redshift (or our best estimate thereof; see Table 1) or the peak of the quasar's Lyα emission. The absence of a significant velocity offset between the halo and the QSO, suggests that we are not witnessing an infall/outflow scenario, e.g., the predictions of Villar-Martín et al. (2007) and Weidinger et al. (2005).

Interestingly, the velocity widths of the emission-line profiles for each halo are very broad, of only marginally lower

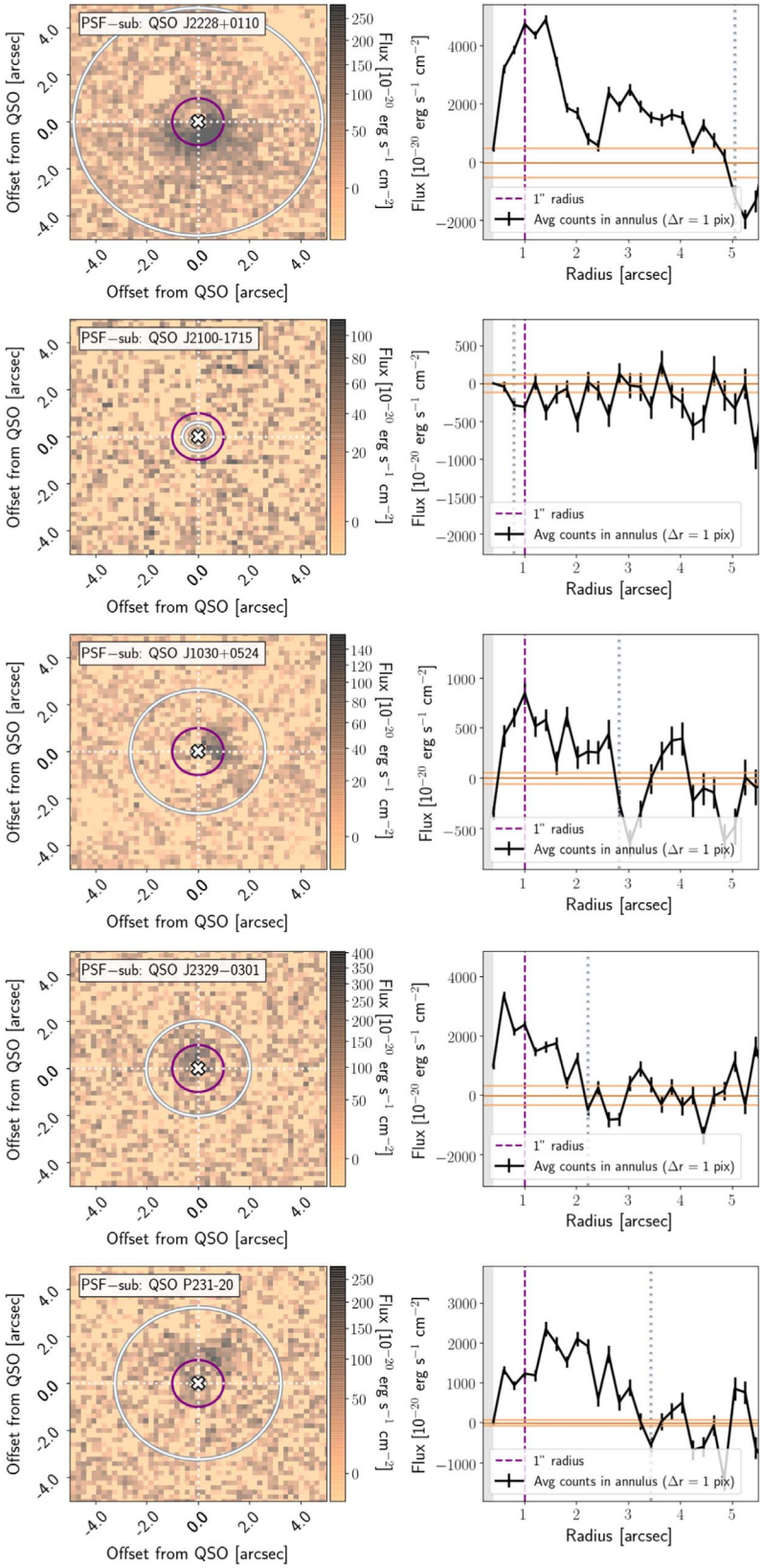

Figure 2. Fixed-width narrowband images centered on the Lyα line and azimuthally averaged radial light profiles. The images in the left column are constructed such that they encompass the spectral width of the Lyα line in the PSF-subtracted cube; details are outlined in Section 4.2.1 and shown in the Appendix. Overlaid is an aperture of 2″ in diameter (purple circle) and an aperture to show the profile radius determined in the adjacent column of panels. On the right side we show each light profile and its 3σ error out to a radius of ∼5″, and exclude the very central region of the profiles, which cannot be trusted due to possible PSF subtraction artifacts (shaded gray). The purple dashed line corresponds to the 2″ diameter aperture, and the gray dashed line indicates the radius where the light profile hits the background of the observations (the dark orange lines represent the background level, and the light orange lines denote the 1σ deviation).

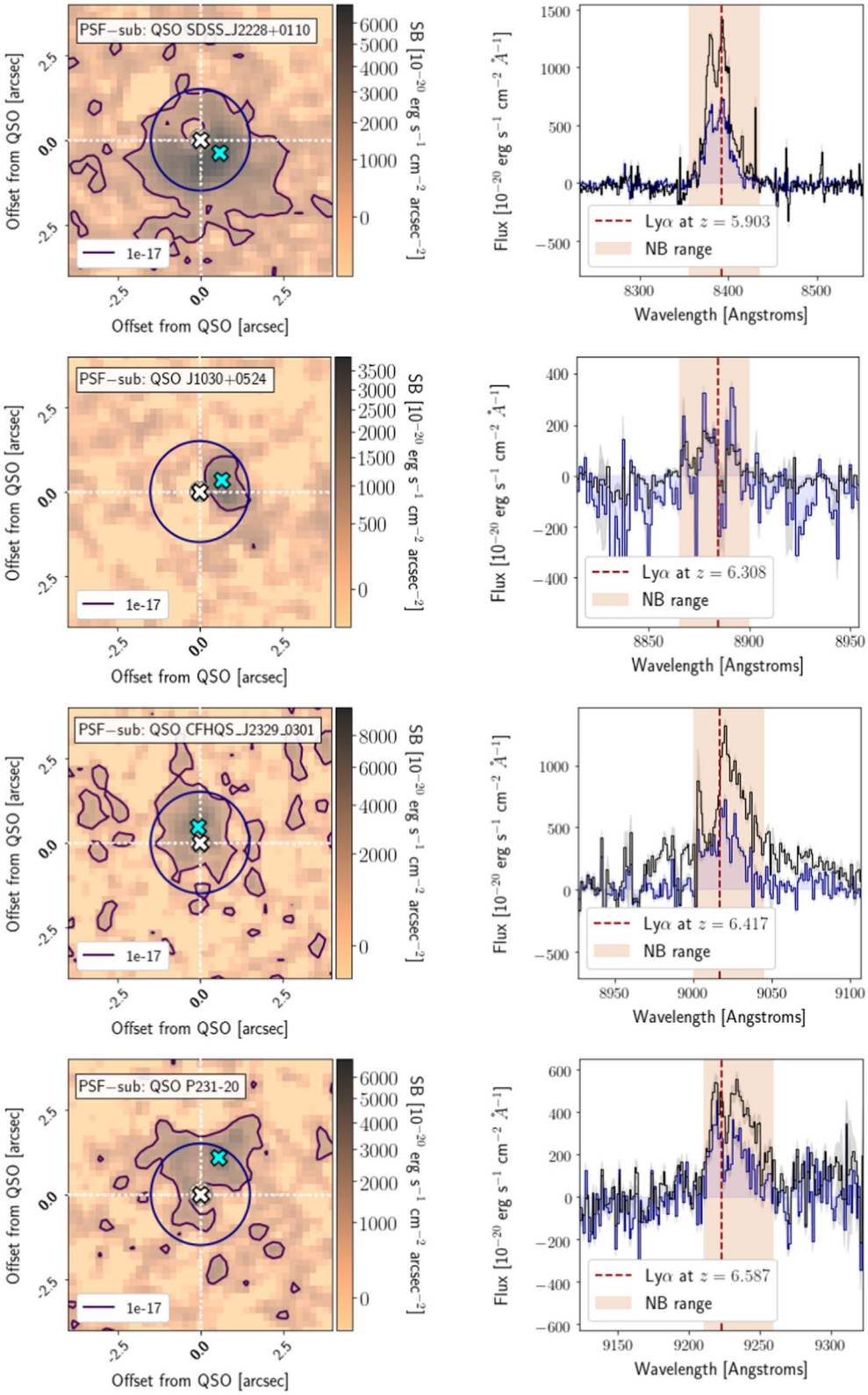

Figure 3. Smoothed surface-brightness images and spectra of the PSF-subtracted Lyα halo. Note that the central 4 pixels (approximately the size of the PSF) have been masked in the datacube and thus do not contribute to the images or spectra shown here. In the left panels we show the same narrowband image as in Figure 2, now smoothed with a Gaussian kernel of $\sigma = 1.2$ pixels, in units of surface brightness, and contoured at a level of SB $= 1.0 \times 10^{-17}$ erg s^{-1} cm^{-2} arcsec^{-2} (black line). On this image we show the quasar position (white cross) and the peak of the Lyα emission in the halo, which remains after PSF subtraction (cyan cross), in addition to an aperture 2″ in diameter. In the right panels we show in blue the spectrum extracted from the PSF-subtracted cube within the 2″ diameter aperture, and overlay in black a spectrum extracted by summing all the voxels (volumetric pixels) lying within the 1.0×10^{-17} erg s^{-1} cm^{-2} arcsec^{-1}2 contour. The dashed red line gives the predicted position of the peak of the Lyα emission according to the systemic redshift of the quasar (Table 1), and the shaded orange region corresponds to the wavelength region that makes up the narrowband image.

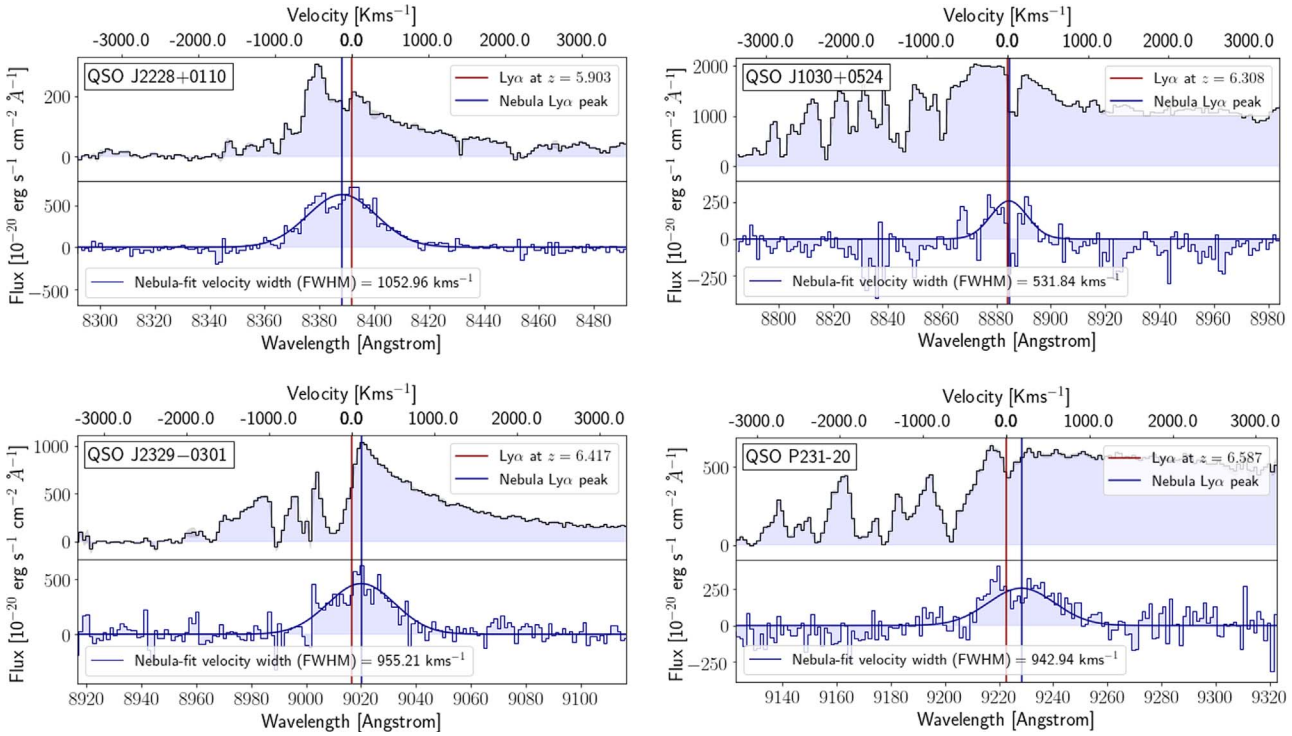

Figure 4. Spectra of each QSO and its Lyα halo. In the upper panels we show the QSO spectrum extracted from the central four pixels (i.e., approximately the size of the PSF). In the lower panels we show spectra of the Lyα halo in the PSF-subtracted datacube in an aperture 3″ in diameter. Note that for the Lyα halo spectra the central four pixels centered on the QSO have been masked from the datacube and do not contribute to the Lyα halo spectrum. Overlaid on each pair of spectra are the predicted position of the Lyα line according to our best estimate of the systemic redshift of the quasar (red line); and the peak of the PSF-subtracted emission (blue line). For each object we fit a Gaussian profile to the PSF-subtracted line to estimate the velocity width. The best-fit FWHM values in km s^{-1} are noted on each panel.

Table 3
Properties of Diffuse Emission of SB $> 1 \times 10^{-17}$ erg s^{-1} cm^{-2} arcsec^{-2}

QSO	Area $> 1 \times 10^{-17}$ (arcsec^2)	Neb Offset (arcsec)	Neb Offset (pkpc)	Vel Offset (km s^{-1})	Vel (km s^{-1})
J2228+0110	18.16	0.69	4.0	−126.25	1052.96
J2100−1715	…	…	…	…	–
J1030+0524	1.47	0.74	4.1	18.46	531.84
J2329−0301	5.92	0.44	2.5	116.18	955.21
P231−20	6.57	1.21	6.5	181.66	942.94

Note. In the first column we give the QSO names. In the second column we present the contiguous area in square arcseconds that is above SB $> 1 \times 10^{-17}$ erg s^{-1} cm^{-2} arcsec^{-2}. In the third and forth columns we give the spatial offset of the peak of the halo emission from the position of the QSO, in arcseconds and pkpc. In the fifth column we give the velocity offset of the halo from the QSO, and in the final column we give the velocity width (FWHM) of the Lyα line arising from the halo.

velocity width than the Lyα from the QSO. This is an interesting contrast from the halos seen in Borisova et al. (2016), yet it is strikingly similar to the case seen in Ginolfi et al. (2018).

4.3.3. Spatially Resolved Kinematics

In contrast to the integrated values, spatially resolved kinematic maps provide insight into the internal kinematics of the halos (as opposed to the bulk motion relative to the quasar discussed above in Section 4.3.2).

We keep the wavelength layers chosen in Section 4.2, smooth the datacube in the two spatial directions with a Gaussian kernel of $\sigma = 1.0$ pixel, and threshold the individual voxels (volumetric pixels) according to their S/Ns. In the first column of panels of Figure 5 we show the zeroth-moment (flux images) that satisfy our S/N cut, i.e., the voxels that make up the remainder of the kinematic analysis.[8] Keeping all voxels with S/N > 2.0 we calculate the first- and second-moment maps. Again, much as in Borisova et al. (2016) and Arrigoni Battaia et al. (2019), we do not assume any particular form of the Lyα line (i.e., we do not attempt to fit a Gaussian profile), and instead compute the non-parametric flux-weighted moments.

In the central column we show the first moment, i.e., the flux-weighted velocity of the halos relative to the peak of the Lyα emission from the halo, to provide information on the internal velocity structure of the halos. In these maps we can search for any sign of ordered motion—although the Lyα line

[8] Note that these images are distinct from the earlier fixed-width narrowband images, as now each spatial pixel is made up of a different number of wavelength layers that meet the S/N criterion.

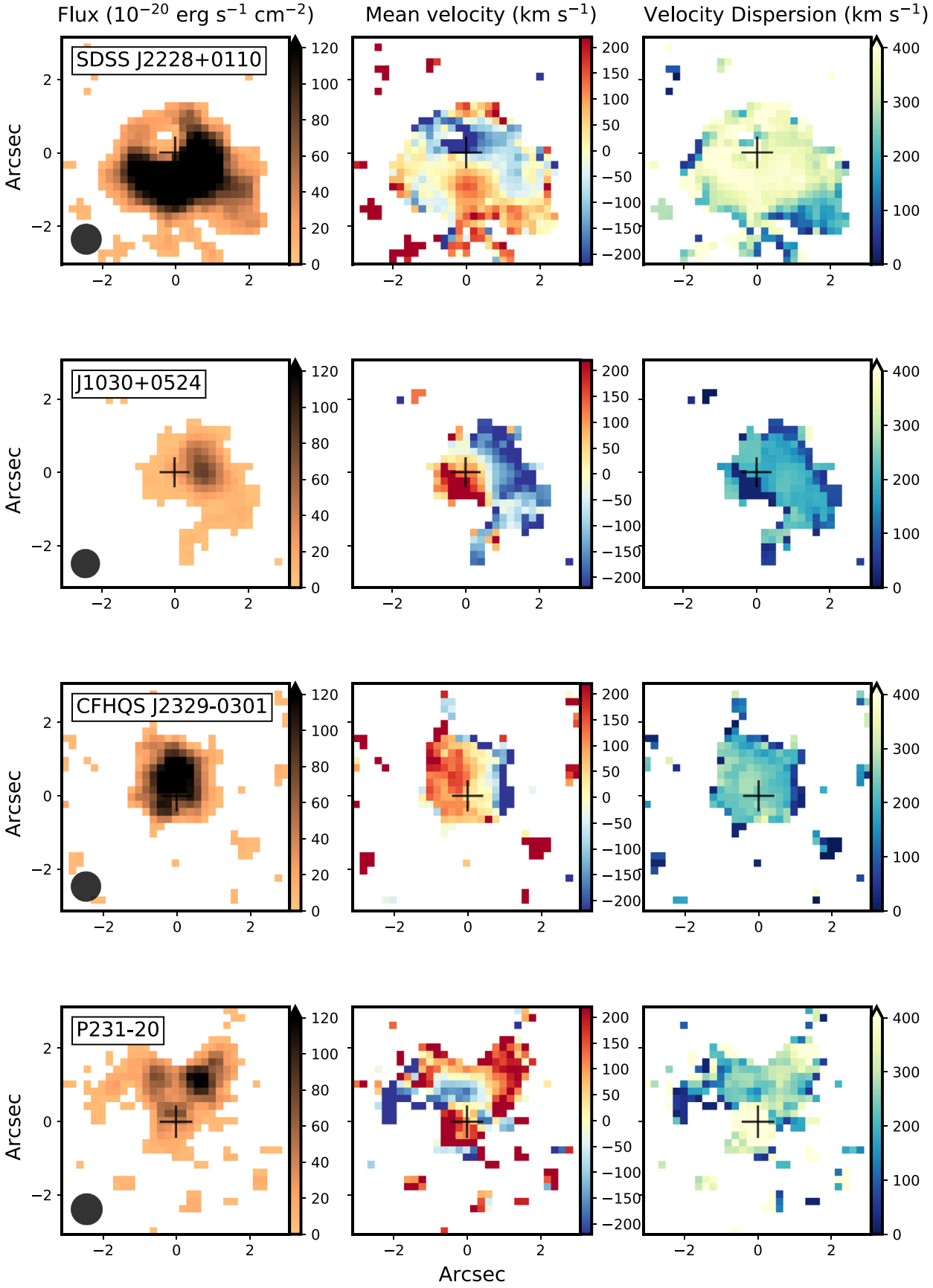

Figure 5. Lyα moment maps for the PSF-subtracted halos around each of the quasars. In the left column we show moment zero (flux images) containing all volumetric pixels with a S/N $\geqslant$ 2, that make up the rest of the kinematic analysis. In the central column we show the first moment, i.e., the velocity of each spatial pixel relative to the peak of the halo Lyα emission, and in the right column we show the second moment, or velocity dispersion in each spatial pixel. The details of the routine are given in Section 4.3.3.

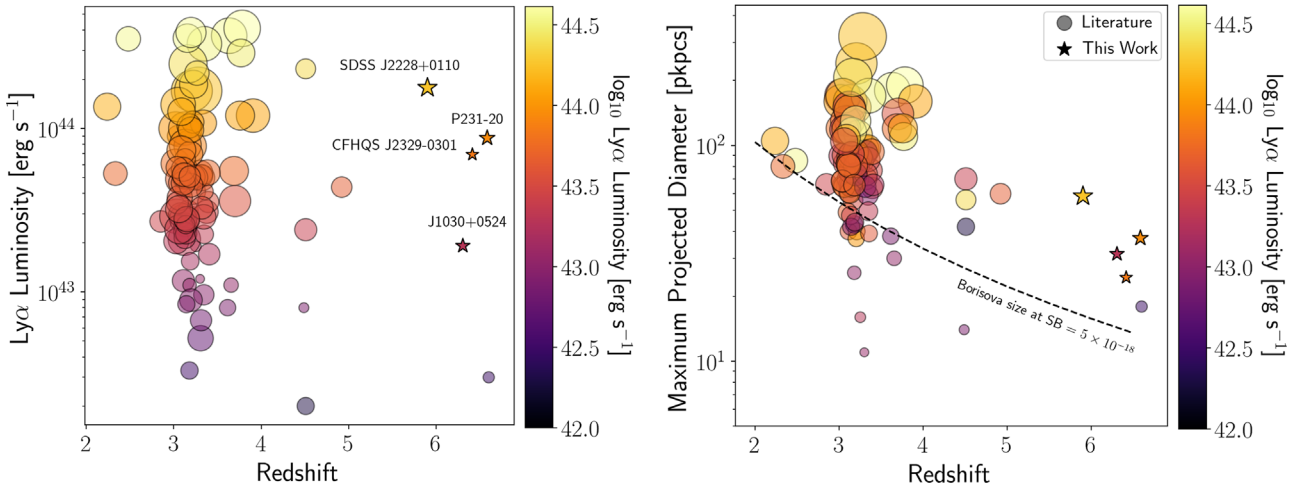

Figure 6. Total Lyα luminosities and sizes of Lyα halos surrounding QSOs plotted as a function of their redshifts. In each panel we show a compilation of literature sources from Arrigoni Battaia et al. (2019) and Borisova et al. (2016) (circular symbols) across the redshift range $2 < z < 5$. At redshift $z > 6$ we show the data point from Farina et al. (2017), and the measurements presented in this work (star symbols). In each panel we plot halo redshift on the abscissa, and a commonly measured halo property on the ordinate; the left panel shows measured total halo luminosities, and the right panel shows the measured maximum projected diameters in proper kiloparsecs, overlaid with a dashed line to show the apparent size of a typical Borisova et al. (2016) halo with redshift at our sensitivity limit. Size and luminosity information is also encoded in both panels as the size of the plotted points, and their colors, respectively.

is not necessarily the best tracer of gas motion due to complex radiative transfer issues, we can use the velocity offset of the emission to look for any obvious signatures.

The four halos present a complex picture that is difficult to interpret. Each halo shows a velocity gradient across its spatial extent, indicating some movement in the gas, with total velocity ranges of $\Delta v \sim 400\,\mathrm{km\,s^{-1}}$ (i.e., $\pm 200\,\mathrm{km\,s^{-1}}$ relative to the peak of the Lyα from the halo).

In the case of J2228+0110, the only known radio-loud quasar in the sample, the gradient occurs in an east-west direction (i.e., *not* varying with distance from the quasar) and with a slight warp. J1030+0524, on the other hand, displays a tentative velocity gradient with distance from the quasar, and gas at the spatial position of the quasar is redshifted by $\sim 200\,\mathrm{km\,s^{-1}}$, but by the outer extents of the halo has shifted to $\sim -200\,\mathrm{km\,s^{-1}}$. J2329−0301 again shows some signs of ordered motion, with a velocity gradient and warp. Finally, P231−20, the highest-redshift object in our sample, displays some complex patterns. The quasar resides toward the south of the halo, with a patch of redshifted emission below it. North of the quasar the emission is blueshifted, however, and further north the offset blobs of emission are again redshifted ($\sim 200\,\mathrm{km\,s^{-1}}$) relative to the quasar.

In the right column of images we show the second moment, or velocity dispersion σ, within the halos.[9] Each halo shows a very broad Lyα line. The radio-loud quasar J2228+0110 does display the highest velocity dispersion, as one might expect following literature results such as Borisova et al. (2016) and Ginolfi et al. (2018). The next two highest-redshift objects in our sample, J2100−1715 and J1030+0524, both show a lower velocity dispersion. J2100−1715 appears to show uniform values across its full extent, whereas for J1030+0524 larger velocity dispersions are seen closer to the position of the quasar. Finally, P231−20 again displays complex information. Here, the quasar is certainly centered in the region of highest-velocity dispersion, but there is a secondary peak in the image at the position of the large blob of emission in the northwestern direction.

5. Discussion

5.1. Comparison to Lower-redshift Samples

Many results in the literature have noted that Lyα SB profiles, halo Lyα luminosities, and maximum projected sizes show smaller values at $z \sim 6$ than at lower redshift. In Figure 6 we present our measured Lyα halo luminosities and maximum projected sizes in the context of a compilation of literature sources. We include in the plot Lyα halos around all QSOs (both radio-loud and radio-quiet) from Borisova et al. (2016) and Arrigoni Battaia et al. (2019), in addition to the compilation presented in the PhD thesis of Arrigoni Battaia[10] across the redshift range $2 < z < 5$. At redshift $z > 6$ we show the measurements presented in this work, and the data point from Farina et al. (2017).

5.1.1. Evidence for Luminosity Evolution?

Our measurements show little evolution of the luminosity of Lyα halos with redshift. This is in contrast to previous measurements at $z \geqslant 6$. Our re-analysis of J2228+0110 in the MUSE datacube places its luminosity an order of magnitude higher, and likewise, J1030+0524, which previously was not reported to display a Lyα halo, now appears with a small halo of moderate luminosity that is an order of magnitude more luminous than Farina et al. (2017). This stresses the need for larger samples of Lyα halos around QSOs at $z \sim 6$.

5.1.2. Evidence for Size Evolution?

On the right side of Figure 6 we show the maximum projected diameters of our sample and those in the literature.[11]

[9] Note that here we are displaying σ, and not the Gaussian-equivalent FWHM value in each pixel (frequently, 2.35 times σ is used in the literature.)

[10] https://www.imprs-hd.mpg.de/49473/thesis_Arrigoni.pdf

[11] Note: we now discuss *diameters* of the halos by taking 2× the maximum radial projections measured in this work. This is for consistency with literature results, despite the fact that many reported halos, and all those presented in this work, are asymmetric.

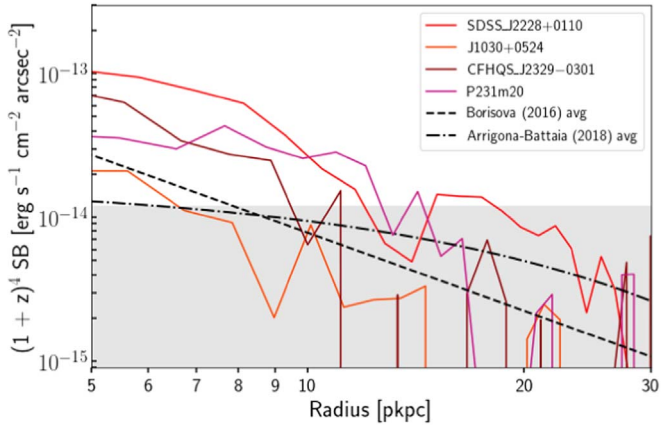

Figure 7. Azimuthally averaged, surface-brightness profiles in proper kiloparsecs corrected for surface-brightness dimming (i.e., expressed in units of observed SB $\times (1+z)^4$) for each of our objects. The shaded region indicates our surface-brightness limit. We overplot the average profiles of Borisova et al. (2016) and Arrigoni Battaia et al. (2019).

The plot appears qualitatively similar to Figure 6 of Ginolfi et al. (2018), who also noted the apparent trend of increasing maximum projected size toward lower redshifts. This size evolution is also corroborated by Momose et al. (2019), who argued that the Lyα halo sizes scale with the size of evolving dark matter halos. Although we confirm with our data that the proper sizes are smaller at higher redshifts, we do not propose any specific scaling in this work.

We next compare our measurements to the average surface-brightness profile measured in Borisova et al. (2016) at $\langle z = 3.2$. If we assume that this halo is typical of quasar (Lyα) halos across cosmic time, we can predict its appearance at redshift z in observations reaching our average surface-brightness limit (for the sources measured in this paper, the sizes are measured on a background of a $(\sim 3\text{–}7) \times 10^{-18}$ erg s^{-1} cm^{-2} arcsec^{-2} see Table 2). For instance, we can see from Figure 6 that at $z \sim 6$ the value of the Borisova et al. (2016) halo's maximum projected diameter would be measured as $\leqslant$15 pkpc in observations reaching a surface-brightness level of SB $\sim 5.0 \times 10^{-18}$ erg s^{-1} cm^{-2} arcsec^{-2}. This means that each of the Lyα halos presented in this work appears larger than a typical Borisova et al. (2016) halo would appear placed at $z \sim 6$.

5.1.3. Evidence for Surface-brightness Profile Evolution?

In Figure 7 we present the azimuthally averaged surface-brightness profiles of each of the quasars presented here. We show the surface-brightness-dimming-corrected profiles (i.e., SB$_{\rm obs} \times (1+z)^4$) on a scale of proper kiloparsecs (pkpc). The gray shaded area shows our surface-brightness sensitivity. A comparison to Borisova et al. (2016) and Arrigoni Battaia et al. (2019) shows that we would not have detected their average profiles in our observations.

5.2. Physical Origin of Lyα Emission

In order to determine the energy source and spatial origin of the Lyα emission observed here as a halo, we need additional line diagnostics from the same gas. With Lyα alone, we can only use the velocity width and spatial extent on-sky to speculate the physical processes at work. In addition, we can use previous observations of the QSOs to look for any correlation between the observed properties of the QSOs and the Lyα halos.

In Figure 8 we plot for each source its halo luminosity against an observable commonly used to characterize the quasars themselves. In the left panel we show Lyα halo luminosity against M_{1450} as a proxy of the black hole mass. The scatter of the measurements in this plot implies that the Lyα halo is not in fact directly linked to or influenced by the black hole. Indeed, J2100−1715, which displays no halo above the limit of our observations, is firmly toward the middle of the range of M_{1450} values, as is the data point from Farina et al. (2017), which displays only a faint halo.[12] In the right panel we show the halo luminosity again against the log of the far-infrared luminosity, tracing obscured star formation. Once again the points show no obvious correlation between star formation activity in the host galaxy and the powering of the Lyα halo. These results point toward a scenario in which the Lyα halo emission is more closely related to properties of diffuse gas in the CGM/IGM than of the black hole or host galaxies' stellar populations.

5.3. Lyα Emission within R$_{vir}$?

A particularly interesting question is whether we are observing pristine gas in the IGM falling onto the QSOs, or gas that is part of the objects' CGM, i.e., within the virial radii. To make any statement about the extent of the emitting gas with respect to each object's virial radius, we need to make some assumption about the hosting $M_{\rm DMhalo}$. Evidence suggests that black holes are already 10^9 $M_\odot$ at $z \sim 6$ (Mazzucchelli et al. 2017a), and that gas masses are of order 10^{10} $M_\odot$ (Venemans et al. 2017, 2018), and the sum of these components will be $\ll M_{\rm DMhalo}$. As such, we assume a conservative lower limit of $\log_{10} M_{\rm DMhalo} = 11.5$ to compute $R_{\rm vir}$ according to Equation (1) (as in Arrigoni Battaia et al. 2019)

$$R_{\rm vir} = [3M_{\rm DMhalo}/(800\pi\rho_{\rm crit}(z))]^{\frac{1}{3}}, \quad (1)$$

where $\rho_{\rm crit}(z)$ is the critical density at redshift z. For $\log_{10} M_{\rm DMhalo} = 11.5$ at $z = 6$ this gives a virial radius of $R_{\rm vir} \approx 30$ pkpc. Each of the Lyα halos presented in this work displays a maximum radial extent $\lesssim$30 pkpc, meaning that unless the host dark matter halo mass $\ll \log_{10} M_{\rm DMhalo} = 11.5$ (which we consider unlikely), we are observing emission from circumgalactic gas *inside* the virial radius, i.e., not the IGM. To investigate the nature of this gas further (pristine? first infall? outflows?) requires additional diagnostics that are not currently available.

5.4. Lyα Halos Consistent with Evolution Seen at z = 2–3?

Arrigoni Battaia et al. (2019) derived an empirical model of Lyα halo evolution from $z = 3.2$ to $z = 2.25$. They found that the normalization of their surface-brightness profiles decreases by approximately an order of magnitude over this redshift range. Assuming that this trend holds out to $z = 6$, we estimate the resulting profile and compare to our observations in Figure 9, assuming the virial radius estimates from Section 5.3. Our SB profiles fall below such an empirically predicted evolution. This means that the evolution between the average

[12] Note that although black hole mass estimates exist for several of the objects examined here, these rely on additional assumptions, and are derived via different methods for different QSOs depending on the information available, therefore we choose to examine only the M_{1450} proxy for each object.

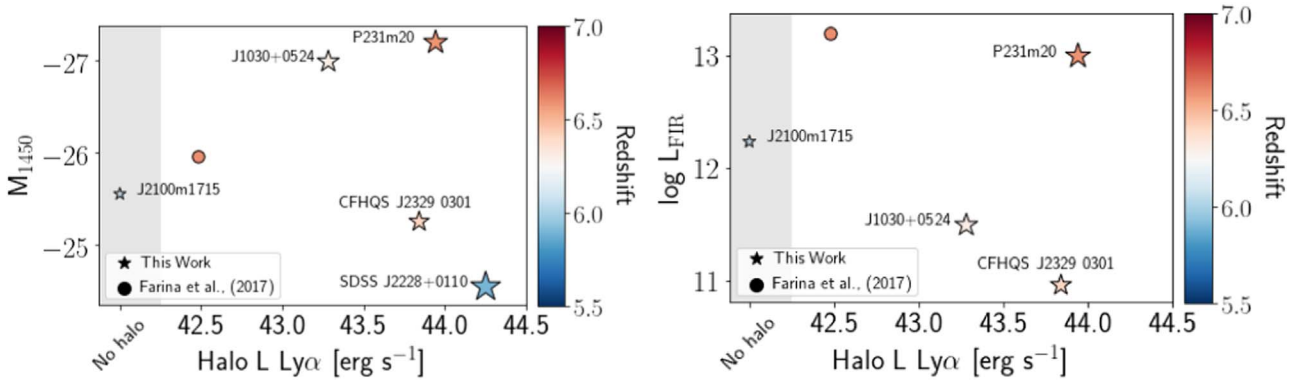

Figure 8. Observed quasar properties plotted against Lyα halo luminosities for all sources presented in this work, and the halo in Farina et al. (2017). In the left panel we show the absolute magnitude at 1450 Å, and in the right panel we show the far-infrared luminosity. Points in each panel are color-coded by redshift.

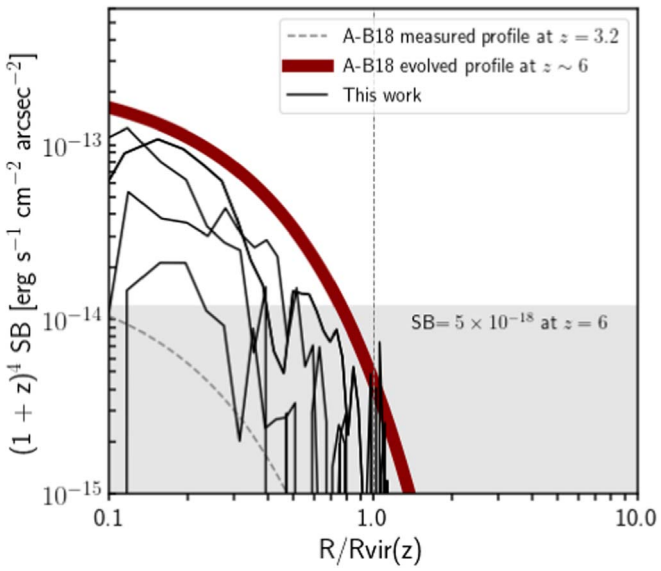

Figure 9. Surface-brightness profiles of our Lyα halos normalized to the virial radius for a dark matter halo of mass $\log M_{\rm DMhalo} = 11.5\, M_{\odot}$ (see the text). We show the Lyα halos measured in this work in thick black lines, and the measured profile of Arrigoni Battaia et al. (2019) at $\langle z = 3.2\rangle$ as a gray dotted line. The thick red band shows the appearance of the Arrigoni Battaia et al. (2019) profile when assuming that the SB profile evolution found by Arrigoni Battaia et al. (2019) at $z = 2$–3 holds out to $z \sim 6$. The surface-brightness profiles are surface-brightness-dimming-corrected (i.e., $[1 + z] \times$ SB) and measured radii are in proper units, normalized to a virial radius calculated according to $R_{\rm vir} = [3M_{\rm DMhalo}/(800\pi\rho_{\rm crit}(z))]^{\frac{1}{3}}$.

SB profile at $z \sim 3$ and $z \sim 6$ is not as strong as that seen between $z \sim 3$ and $z \sim 2$ in Arrigoni Battaia et al. (2019).

6. Conclusions

We present MUSE (archival) data of five $z \sim 6$ QSOs. After PSF subtraction we search for extended Lyα emission in the vicinity of each quasar. For four out of five QSOs we detect extended, diffuse Lyα emission, directly probing the CGM at $z \sim 6$.

Our findings are summarized below:

1. The four Lyα halos presented here are diverse in morphology and size, they each display spatial asymmetry, and none are centered on the position of the quasar.
2. None of the halos are significantly offset in velocity from the systemic redshift of the quasars ($\Delta v < 200\,{\rm km\,s^{-1}}$).
3. Each halo shows a broad Lyα line, with a velocity width of order $1000\,{\rm km\,s^{-1}}$.
4. Total Lyα luminosities range between $\sim 2 \times 10^{43}$ and $\sim 2 \times 10^{44}\,{\rm erg\,s^{-1}}$, reaching maximum radial extents of 13–30 pkpc from the quasar positions.
5. We find larger sizes and higher Lyα luminosities than previous literature results at this redshift that generally did not employ IFU data. This alters the perception that Lyα halos are less luminous at higher redshift.
6. We see no correlation between QSO properties and the characteristics of the Lyα halo and thus infer no evidence that neither black holes nor the stellar populations of host galaxies are the primary driver of the Lyα halo emission at $z \sim 6$.
7. The Lyα emission observed here is located within the virial radius of our targets, assuming a conservative $\log_{10} M_{\rm DMhalo} = 11.5$.
8. The redshift evolution of the SB profiles between $z \sim 6$ and $z \sim 3$ appears to be less pronounced than seen between $z \sim 3$ and $z \sim 2$ in Arrigoni Battaia et al. (2019).

Overall, our results are consistent with a picture in which the physical properties of the CGM evolve with cosmic time, manifesting as an observed evolution of Lyα halo properties. Before this scenario can be confirmed or clarified, a larger sample of QSO observations at $z \sim 6$ is called for, and observations of more diagnostic lines (e.g., with the upcoming *James Webb Space Telescope* mission). This will help to elucidate the processes governing the growth of the first galaxies and black holes.

The authors thank the anonymous referee for insightful suggestions that have improved the quality of this work. A.B.D., M.N., and F.W. acknowledge funding through the ERC grant "Cosmic Gas." A.B.D. acknowledges the MUSE Python Data Analysis Facility, "MPDAF," developed at Centre de Recherche Astrophysique de Lyon. This work is based on observations collected at the European Southern Observatory under ESO programmes: 095.B-0419(A), 297.A-5054(A), 095.A-0714(A), 60.A-9321(A), and 099.A-0682(A).

Appendix

A.1. Choosing the Spectral Window

We include here in Figure 10 the narrowband images and large-aperture spectra from which we chose spectral windows over which to perform photometry.

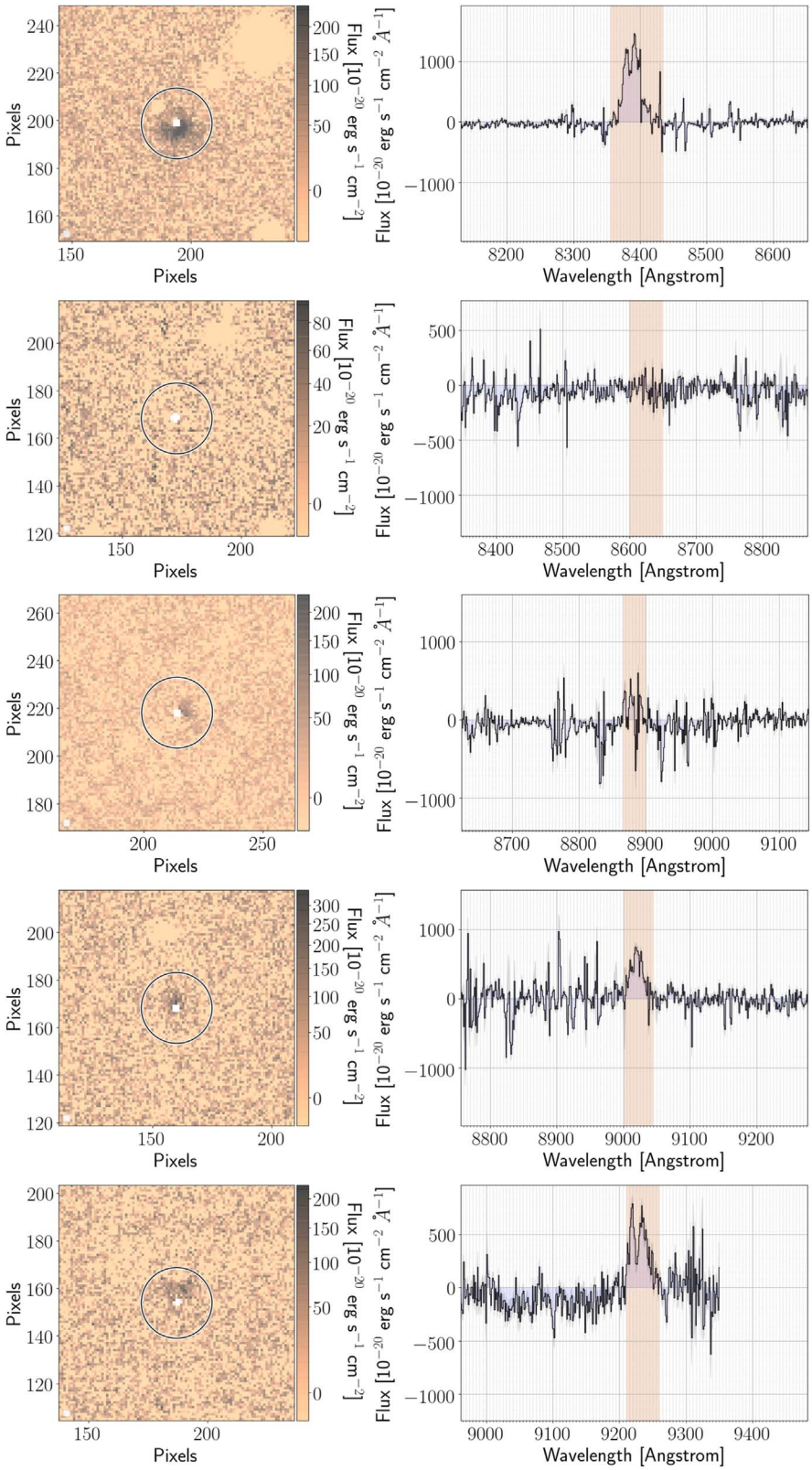

Figure 10. Spectral windows over which we choose to perform photometry of each PSF-subtracted halo. The left panels show narrowband images with an aperture of 6″ overlaid, and the pixels excluded from the Lyα halo analysis due to complex PSF subtraction residuals are masked. The right columns depict spectra extracted from within the 6″ diameter aperture from which the wavelength layers to make up the fixed-width narrowband image were chosen by eye. The wavelength range chosen is highlighted in orange on the spectrum. These wavelength ranges are then propagated to the total flux measurements (Section 4.2.1, and Figure 2), and the surface-brightness images from which we analyze the "bulk properties" of each halo (Section 4.3, and Figure 3).

Appendix B

B.1. White-light Images

As an acillary check, we include here in Figure 11 a white-light collapse of the data cube around each QSO. The images demonstrate that no bright continuum emitters are in close proximity to the QSOs.

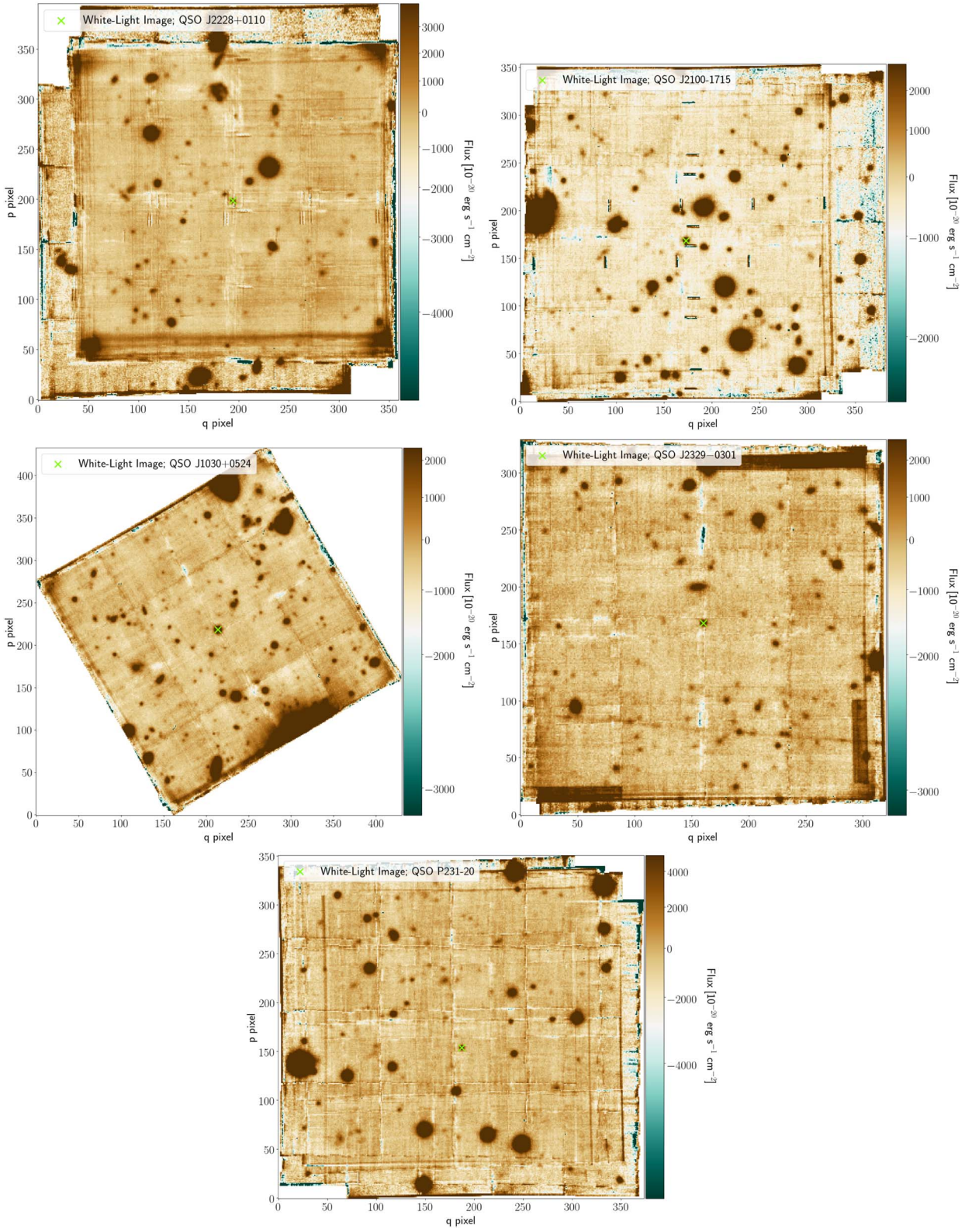

Figure 11. White-light images of each ZAPPED MUSE datacube used in this analysis. In each cutout the quasar is marked by a green cross. The images demonstrate that our measurements are not affected by very bright continuum objects in close proximity to any of the quasars.

ORCID iDs

Alyssa B. Drake https://orcid.org/0000-0002-0174-3362
Emanuele Paolo Farina https://orcid.org/0000-0002-6822-2254
Marcel Neeleman https://orcid.org/0000-0002-9838-8191
Fabian Walter https://orcid.org/0000-0003-4793-7880
Bram Venemans https://orcid.org/0000-0001-9024-8322
Eduardo Banados https://orcid.org/0000-0002-2931-7824
Chiara Mazzucchelli https://orcid.org/0000-0002-5941-5214
Roberto Decarli https://orcid.org/0000-0002-2662-8803

References

Arrigoni Battaia, F., Hennawi, J. F., Prochaska, J. X., et al. 2019, MNRAS, 482, 3162
Bacon, R., Accardo, M., Adjali, L., et al. 2010, Proc. SPIE, 7735, 773508
Bañados, E., Venemans, B. P., Decarli, R., et al. 2016, ApJS, 227, 11
Bãnados, E., Venemans, B. P., Mazzucchelli, C., et al. 2018, Natur, 553, 473
Borisova, E., Cantalupo, S., Lilly, S. J., et al. 2016, ApJ, 831, 39
Cantalupo, S., Arrigoni-Battaia, F., Prochaska, J. X., Hennawi, J. F., & Madau, P. 2014, Natur, 506, 53
Decarli, R., Walter, F., Venemans, B. P., et al. 2017, Natur, 545, 457
Decarli, R., Walter, F., Venemans, B. P., et al. 2018, ApJ, 854, 97
Decarli, R., Walter, F., Yang, Y., et al. 2012, ApJ, 756, 150
Drake, A. B., Garel, T., Wisotzki, L., et al. 2017a, A&A, 608, 6
Drake, A. B., Guiderdoni, B., Blaizot, J., et al. 2017b, MNRAS, 471, 267
Fan, X., Narayanan, V. K., Lupton, R. H., et al. 2001a, AJ, 122, 2833
Fan, X., Strauss, M. A., Richards, G. T., et al. 2001b, AJ, 121, 31
Farina, E. P., Falomo, R., Scarpa, R., et al. 2014, MNRAS, 441, 886
Farina, E. P., Montuori, C., Decarli, R., & Fumagalli, M. 2013, MNRAS, 431, 1019
Farina, E. P., Venemans, B. P., Decarli, R., et al. 2017, ApJ, 848, 78
Ginolfi, M., Maiolino, R., Carniani, S., et al. 2018, MNRAS, 476, 2421
Goto, T., Utsumi, Y., Furusawa, H., Miyazaki, S., & Komiyama, Y. 2009, MNRAS, 400, 843
Goto, T., Utsumi, Y., Walsh, J. R., et al. 2012, MNRAS, 421, 77
Hennawi, J. F., & Prochaska, J. X. 2007, ApJ, 655, 735
Hennawi, J. F., Richards, G. T., Brunner, R. J., et al. 2006, AJ, 131, 1
Kurk, J. D., Walter, F., Fan, X., et al. 2007, ApJ, 669, 32
Leclercq, F., Bacon, R., Wisotzki, L., et al. 2017, A&A, 608, A8
Mazzucchelli, C., Bañados, E., Decarli, R., et al. 2017a, ApJ, 834, 83
Mazzucchelli, C., Bañados, E., Venemans, B. P., et al. 2017b, ApJ, 849, 91
Momose, R., Goto, T., Utsumi, Y., et al. 2019, MNRAS, 488, 120
Roche, N., Humphrey, A., & Binette, L. 2014, MNRAS, 443, 3795
Soto, K. T., Lilly, S. J., Bacon, R., Richard, J., & Conseil, S. 2016, MNRAS, 458, 3210
Tumlinson, J., Peeples, M. S., & Werk, J. K. 2017, ARA&A, 55, 389
Venemans, B. P., Decarli, R., Walter, F., et al. 2018, ApJ, 866, 159
Venemans, B. P., Walter, F., Decarli, R., et al. 2017, ApJL, 851, L8
Villar-Martín, M., Sánchez, S. F., Humphrey, A., et al. 2007, MNRAS, 378, 416
Weidinger, M., Møller, P., Fynbo, J. P. U., & Thomsen, B. 2005, A&A, 436, 825
Willott, C. J., Albert, L., Arzoumanian, D., et al. 2010a, AJ, 140, 546
Willott, C. J., Chet, S., Bergeron, J., & Hutchings, J. B. 2011, AJ, 142, 186
Willott, C. J., Delorme, P., Omont, A., et al. 2007, AJ, 134, 2435
Willott, C. J., Delorme, P., Reylé, C., et al. 2010b, AJ, 139, 906
Wisotzki, L., Bacon, R., Blaizot, J., et al. 2016, A&A, 587, 98
Zeimann, G., White, R. L., Becker, R. H., et al. 2011, ApJ, 736, 57